COMPUTATIONAL STUDY OF A COMPARISON OF CO-FLOW AND COUNTER BLOWING DBD PLASMA ACTUATOR FOR SEPARATION CONTROL OVER AN AIRFOIL

Satoshi SEKIMOTO*
***Department of Aeronautics and Astronautics, University of Tokyo, Kanagawa, Japan**
sekimoto@flab.isas.jaxa.jp

Keywords: *flow separation control, DBD plasma actuator, NACA0015 wing, CFD*

Abstract

Large-eddy simulations of the control of separated flow over an airfoil are conducted, and four types of body force input, co-flow normal input, co-flow burst input, counter-blowing normal input and counter-blowing burst input, are investigared for clarifying the difference of the separation control mechanisms. Comparing the minimum D_c value at which separation can be suppressed, co-flow burst input is most effective, counter-blowing burst input is second effective, and co-flow normal input and counter-blowing normal input are third effective. In co-flow normal input case, co-flow burst input case and counter-blowing burst input case, the spanwise two-dimensional vortices are generated from the leading edge due to Kelvin-Helmholz instability, then they become complex three-dimensional vortices. However, these vortices become three-dimensional vortices more quickly than co-flow normal case. This is because burst mode actuation enhance the instability of the shear layer regardless of the direction of the induced flow. On the other hand, in counter-blowing normal input case, three-dimensional vortices are generated from the leading edge. This is because the large momentum addition disturbs the flow directly. Furthermore, these results are compared with the experiments[1]. Focusing on the reattach point, in both burst cases, the reattach point moves to upstream with increasing D_c value. This result is consistent with that of the experiments.

1 Introduction

Some micro devices for active flow control, such as a synthetic jet or a single dielectric barrier discharge (DBD) plasma actuator(hereafter plasma actuator), get a lot of attentions because they can control separated flow with very small input energy and they can be used flexibly.

A plasma actuator consists of two electrodes separated by a dielectric layer as shown in Fig. 1 [2, 3, 4, 5]. The two electrodes are connected to alternate current (AC) high voltage source, and plasma is generated by dielectric barrier discharge between the exposed electrode and the dielectric layer. This plasma generates flow around the actuator and the induced flow is expected to be used for flow control. It has already revealed that a plasma actuator has good performance for the separation control for low Reynolds number ($Re < 1.0 \times 10^6$) [6]. Several researchers have reported that burst mode input (with duty cycle) for a co-flow plasma actuator generates a good separation control capability in spite of the reduction of the input energy compared with normal mode input. [7] Here, the normal mode input represents the actuation with steady alternative current (AC) input and the burst mode input represents the actuation with the AC input switched on and off periodically as shown in Fig. 2.

Nonomura et al. [8] suggested two types of mechanism for separation control. One type is

direct addition of momentum to the separated region, and the other is induction of freestream momentum due to the enhancement of fluctuation. Also, they compared a co-flow blowing actuator (hereafter co-flow actuator) and a counter flow blowing actuator (hereafter counter flow actuator) in normal mode and burst mode, and reported that co-flow actuation has more effective than counter flow actuation both in normal mode and in burst mode. This result suggests that co-flow actuation might better for separation control than counter flow actuation. However, Visbal et al. [9] reported that a counter-blowing input induced an abrupt transition to turbulence and exploited to delay stall of a NACA0015 wing section for low Reynolds number condition from computational simulations. Porter et al. [10] conducted boundary layer experiments using a co-flow actuator and counter flow actuator, and reported that a counter flow actuation could transition the boundary layer more easily than a co-flow actuation. The result of Nonomura et al. and that of Visbal et al. and Porter et al. seem to be inconsistent. To be accurate, however, above three conclusions are not inconsistent because the target of flow is different. The reason why the characteristics of control of these two different flows differ has not been clarified.

In this study, the separated flow over an airfoil is focused on because there are fewer researches on the investigation of co-flow and counter-blowing flow input and its mechanism has not been clarified, compared to the control of transitional flow over flat plate. Because the flow field in which a plasma actuator is applied is so unsteady and the velocity induced by the body force is very small, implicit large-eddy simulation using sixth-order compact difference scheme is adopted.

2 Computational conditions and setup

2.1 Computational model

The flow conditions are set the same ones as in the previous experimental study [1, 8]. The free-stream Mach number is set to 0.2 and the

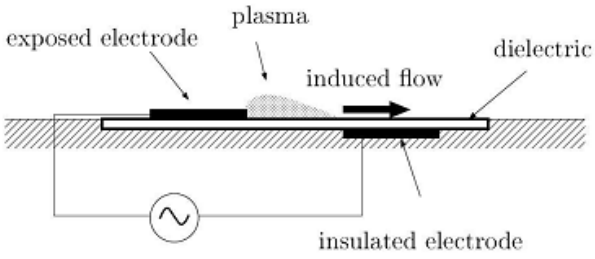

Fig. 1 Configuration of the DBD plasma actuator.

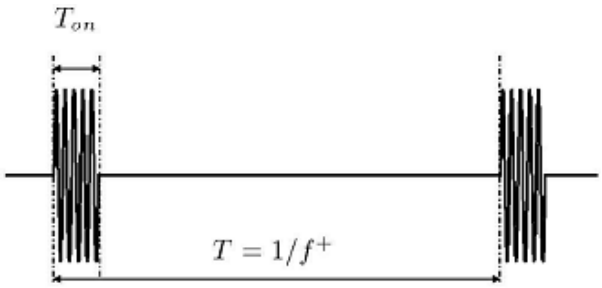

Fig. 2 Unsteady duty cycle.

Reynolds number, on the basis of the chord length, is set to 6.3×10^4. A NACA0015 airfoil is used with the angle of attack 14[deg]. The same body force model is used in all the cases and installed at 5% of the chord length from the leading edge.

2.2 Computational method

The governing equations are three-dimensional Navier-Stokes equations with the body force and the power by the DBD plasma actuator. The body force and the power are modeled with $D_c Q_c E_i (= D_c S_i)$ and $D_c Q_c u_k E_k (= D_c u_k S_k)$ Here, S_i denotes the nondimensional body force vector, Q_c denotes the electric charge, and E_i denotes the electric-field vector. The nondimensional plasma scale parameter D_c is defined as

$$D_c = \frac{Q_{c,ref} E_{ref} c}{\rho_\infty u_\infty^2} \tag{1}$$

where the subscript ref denotes the reference value. Here, $Q_{c,ref}$ and E_{ref} are set as maximum value of Q_c and E in the simulation results for the Suzen model [11]. The nondimensional

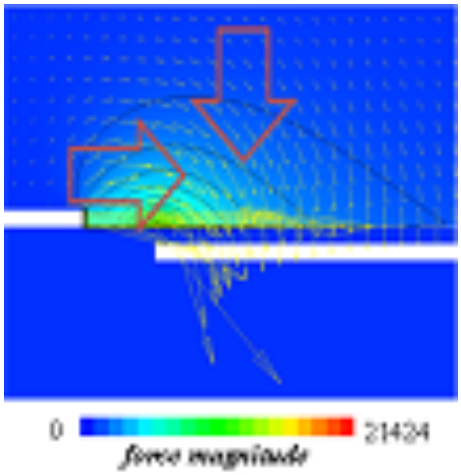

Fig. 3 Force image of Suzen model.

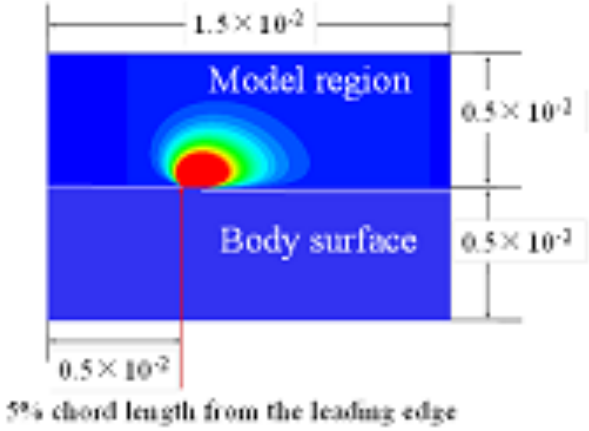

Fig. 4 Force distribution of Suzen model.

plasma scale parameter D_c in this study is similar to previous studies. $D_c = 8$ corresponds to actuation in which the maximum induced velocity becomes approximately equal to the freestream velocity. Figures 3 and 4 show the body force vector distribution of the Suzen model and the body force magnitude distribution for the computation in this paper. The body force in the span direction is set to zero. This body force model is rotated around the point indicated by the red arrow and is installed on the airfoil surface at 5% of the chord length from the leading edge. In counter-blowing actuation case, all the body force vectors are reversed in the chord direction.

In this study, LANS3D[12, 13], a fluid analysis solver developed at ISAS/JAXA, is eployed for the calculations of three-dimensional compressive Navier-Stokes equations. As the velocity induced by the body force is very small and unsteady, a high resolution unsteady computational method is required. Thus, the spatial derivatives of the convective terms and viscous terms, metrics, and Jacobian are evaluated by the sixth-order compact difference scheme[14]. Near the boundary, second-order explicit difference schemes are used. The tenth-order filtering[15, 16] is used with filtering coefficient 0.47. For time integration, a kind of implicit method Lower-Upper Symmetric ADI-SGS[17] is used, where backward second order difference formula is used and three sub-iterations[18] are adopted to ensure the time accuracy. The computational time step is 4×10^{-5} in nondimensional time to obtain a maximum Courant-Friedrichs-Levy (CFL) number of approximately 1.7. In a standard LES approach, additional stress and heat flux terms are attended, but in an implicit-LES approach[19], they are not appended. In this study, implicit-LES approach is adopted and a high-order low-pass filter selectively damps only poorly resolved high frequency waves. This filtering regularization procedure provides an attractive method for the use of standard sub-grid-scale (SGS) models. At the outflow boundary, all variables are extrapolated from one point in front of the outflow boundary. For the airfoil surface, no-slip conditions are adopted. A periodic boundary condition is applied to the boundaries in the spanwise direction.

2.3 Actuator operating conditions

Table 1 shows the computational cases in this research. In co-flow actuation cases, the velocity is induced to downstream direction, where the velocity is induced to upstream direction in counter-blowing actuation cases. In all the cases, the nondimensional base frequency F_{base} is maintained at 160, which is much higher for flow fluctuation and appears to be in steady actuation. In all burst actuation cases, burst ratio BR is 25% and nondimensional burst frequency F^+ is 20.

Table 1 Computational cases

	P/A geometry	drive mode [Hz]	D_c
COF-N8	co-flow	normal	8
COF-N12	co-flow	normal	12
COF-B4	co-flow	burst	4
COF-B8	co-flow	burst	8
INV-N8	counter-blowing	normal	8
INV-N12	counter-blowing	normal	12
INV-B8	counter-blowing	burst	8
INV-B12	counter-blowing	burst	12

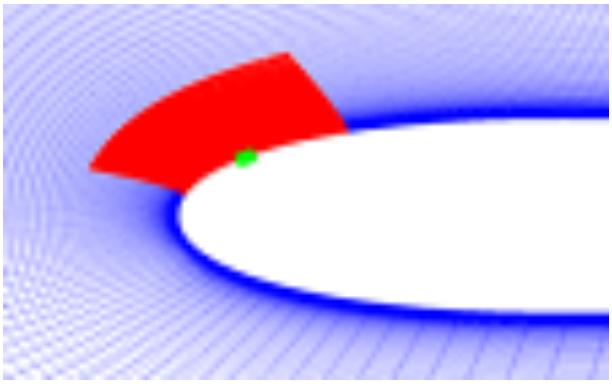

Fig. 5 Computational grids near the leading edge.

2.4 Computational grids

The zonal method is employed to treat the small body force. Figure 5 shows the computational grids, where the body force model is applied at 5% of the chord length from the leading edge. The grids consists of two parts: a blue airfoil grid (zone 1) and a fine red grid (zone 2). Firstly, the body force of the Suzen model is calculated on the green grid corresponding to the body force model region. Then, the body force is mapped to the zone 2 from the green grid. Then, the three-dimensional Navier-Stokes equations are solved in zone 1 and zone 2, and interpolate the physical values between two zones. Zone 1 is a C-type grid and the length from the airfoil surface to the exterior boundary is 20 times chord length. The length of the computational region in the span direction is $0.18c$. The total number of the grid point is $10,400,172$ (351(chordwise) $\times$ 101(spanwise) $\times$ 121(normal)[zone1] & 301(chordwise) $\times$ 101(spanwise) $\times$ 201 (normal)[zone2]). The minimum grid size in the direction normal to the airfoil surface is $1.2 \times 10^{-4}c$

2.5 Validity of Computation

Asada and Fujii compared the C_p distributions of computation results with those of experimental results in order to validate the computational method, and these results agreed with the experimental result[20]. In this research, the same computational code is adopted, and it is reliable to enable a comparison of the qualitative difference in separation control of the body force.

3 Results and Discussions

3.1 Time-averaged flow-fields

In this section, the flow fields, which are averaged in time and spanwise direction, are discussed. Figures 6 show the distributions of averaged chordwise velocity and averaged stream lines at $\alpha = 14$ deg. Comparing $D_c = 8$ cases (COF-N8, COF-B8, INV-N8 and INV-B8), as shown in Figs. 6 (a) and (e), the flow separates at the leading edge in COF-N8 and INV-N8 cases. In COF-B8 and INV-B8 cases, large separation from the leading edge is suppressed. However, the flow is separated from the surface at the center of the wing chord in INV-B8 case. In Figs. 6 (b), (f) and (h), the results of $D_c = 12$ cases of co-flow normal input, counter-blowing normal input and counter-blowing burst input (COF-N12,INV-N12 and INV-B12), in which separation is not fully suppressed, are shown. These figures shows that separation is suppressed in these three cases. Figure 6 (d) shows the results of co-flow burst mode actuation with $D_c = 4$ case (COF-B4). Also in this case, separations at the leading edge is suppressed.

Figures 7 and 8 show the C_p distributions on the airfoil surface in co-flow input cases and counter-blowing input cases respectively. The separated region, shown in Figs. 6, is also ob-

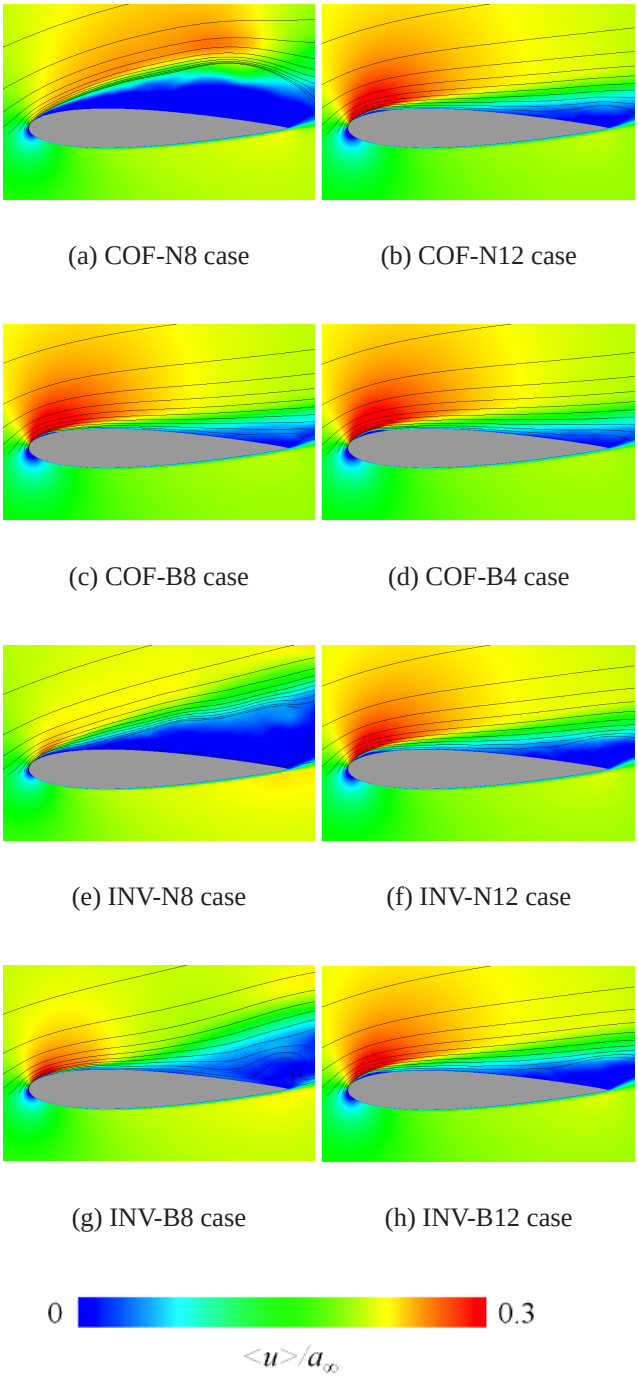

Fig. 6 Time-averaged and spinwise-averaged chord direction velocity distributions with stream lines.

served in these C_p distributions. In the COF-N8 and INV-N8 cases, C_p is distributed with a plateau on the suction surface and is less than zero at the trailing edge. This means that the flow separates from the leading edge and does not reattach. The other cases have separated regions, where C_p distribution has a plateau near the leading edge, although INV-B8 case has higher C_p value than other cases in which separation is fully suppressed. In addition, near 5% of the chord length, there are small steps in co-flow normal mode cases (COF-N8 and COF-N12), and there are small peaks in counter-blowing normal mode cases (INV-N8 and INV-N12). This is because the velocity is induced in co-flow normal input cases and reduced in counter-blowing normal input cases by the body force. Thus, these steps and peaks near 5% of the chord length becomes larger as the D_c value, which is proportional to the body force, becomes higher. And burst mode input cases have no or relatively small steps and peaks. Furthermore, the peak value of C_p near the leading edge in the co-flow input cases is higher than that in the counter-blowing input cases. This is because the attached flow is accelerated in the co-flow input cases, where it is not accelerated or, on the contrary, decelerated in the counter-blowing input cases by the body force.

Figures 9 and 10 show the C_f distributions on the suction surface in co-flow input cases and counter-blowing input cases respectively. Near 5% of the chord length, co-flow input cases have positive peaks, where counter-blowing input cases have negative peaks. This is because the flow near the surface is induced to the downstream direction in the co-flow input cases and to the upstream direction in counter-blowing input cases by the body force. As shown in Figs. 9 and 10, the flows in COF-N12,COF-B8,COF-B4,INV-N12,INV-B8 and INV-B12 cases reattach, and the flows in the other cases do not.

Figures 11 show $-u'w'$ corresponding to the Reynolds stress distributions. The high $-u'w'$ region is distributed in the region where two-dimensional vortices are generated from the separated shear layer. The COF-N8, INV-N8 and INV-B8 cases have wide high $-u'w'$ region. In

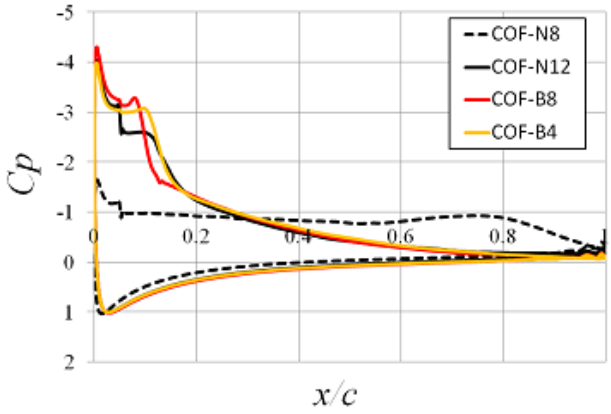

Fig. 7 C_p distributions of co-flow input cases.

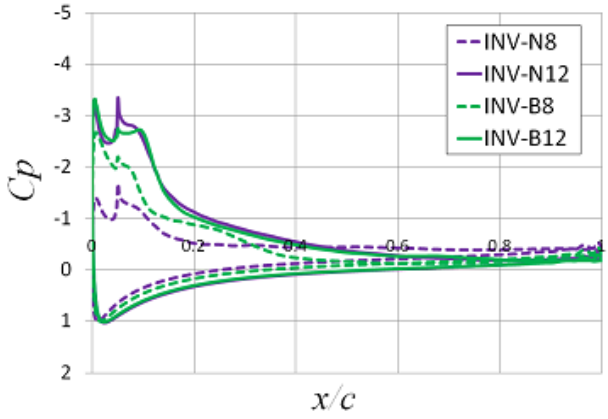

Fig. 8 C_p distributions of counter-blowing input cases.

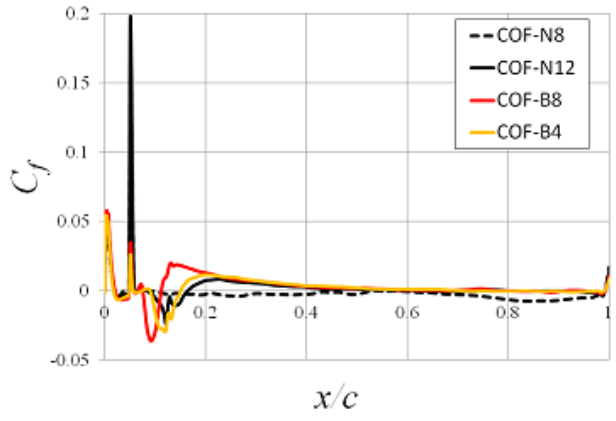

Fig. 9 C_f distributions of co-flow input cases.

the other cases in which the flow is fully attached, the $-u'w'$ distributions seems to have almost the same characteristics, although high $-u'w'$ region near the trailing edge of co-flow input cases is closer to the surface than that of counter-blowing input cases. Focusing on near 5% of the chord length where the body force is applied, burst mode input cases (COF-B4,COF-B8,INV-B12) have relatively high $-u'w'$ region compared to normal mode input cases (COF-N12, INV-N12).

Thus, in terms of separation control, burst mode input cases are more effective than normal mode input cases regardless of the direction of the induced flow, and co-flow burst input can suppress separation with smaller D_c value than other cases. The results of Figs. 11 seem to imply that the main factor for separation control is not the same between four actuations, co-flow normal input, co-flow burst input, counter-blowing normal input and counter-blowing burst input. In the next subsection, we discuss about the main factor for separation control for each case with the instantaneous flow fields.

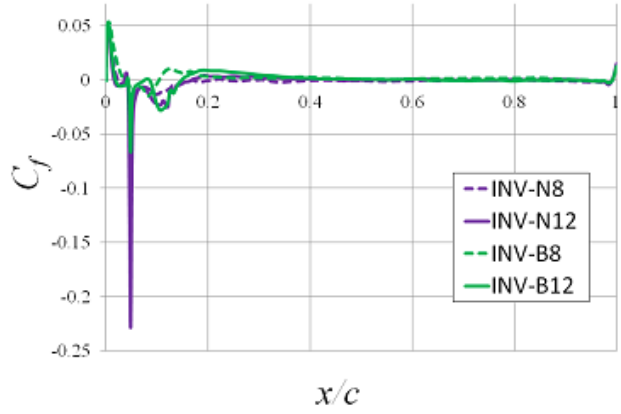

Fig. 10 C_f distributions of counter-blowing input cases.

3.2 Instantaneous flow-fields

Figures 12 show the instantaneous flow fields of the COF-N12,COF-B4,INV-N12 and INV-B12 cases, in which the separation is considered to be fully suppressed. In each figure, the iso-surface shows the second invariant of the velocity gradient tensors colored by x-vorticity. The background is colored by the chord directional velocity. In the COF-N12 case, the

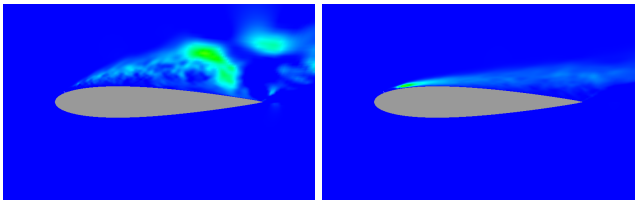

(a) COF-N8 case (b) COF-N12 case

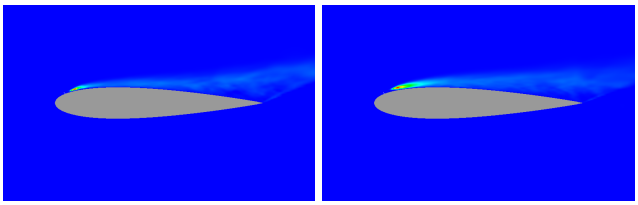

(c) COF-B8 case (d) COF-B4 case

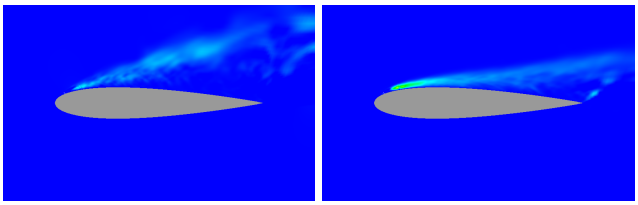

(e) INV-N8 case (f) INV-N12 case

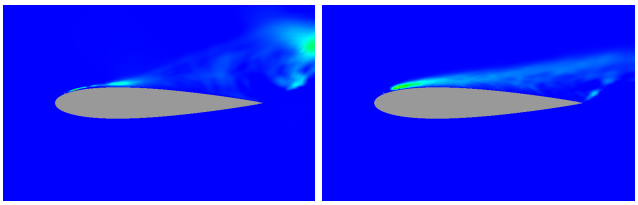

(g) INV-B8 case (h) INV-B12 case

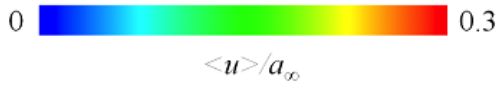

Fig. 11 Reynolds stress distributions.

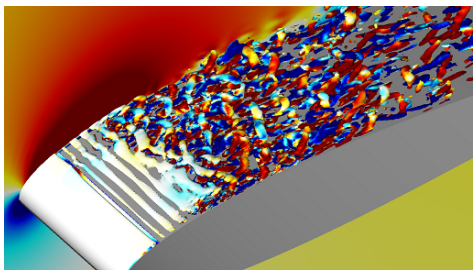

(a) COF-N12 case

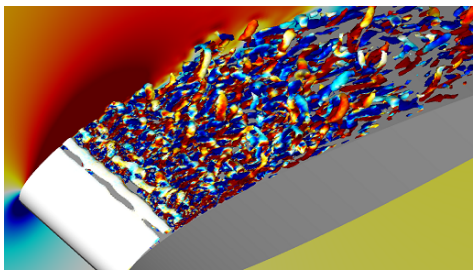

(b) COF-B4 case

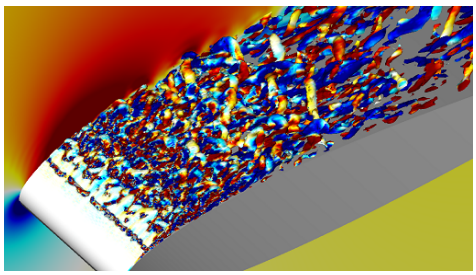

(c) INV-N12 case

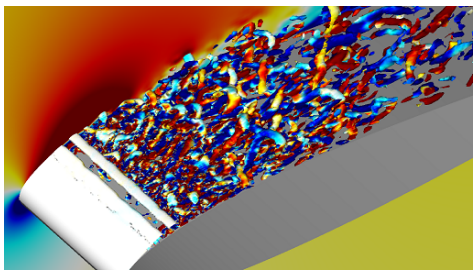

(d) INV-B12 case

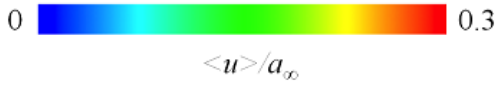

Fig. 12 Instantaneous isosurface of the 2nd invariant pf velocity gradient tensors and chord direction velocity distributions.

spanwise two-dimensional vortices are generated from the leading edge due to Kelvin-Helmholtz instability. These vortices break down and become complex three-dimensional turbulent vortices, then reattach occur. In the COF-B4 case, two-dimensional vortices are also generated near the leading edge. However, these vortices become three-dimensional vortices more quickly than in the COF-N12 case. Also in the INV-B12 case, two-dimensional vortices are generated near the leading edge and quickly become three-dimensional vortices. On the other hand, in the INV-N12 case, fine three-vortices, instead of two-dimensional vortices, are generated near the leading edge.

From the results above, it is considered that there are several mechanisms for separation control, as Nonomura suggested[8]. In the co-flow normal mode case, it is considered that shear layer is constrained to the surface by the direct momentum addition of the body force. Considering that the cases of co-flow burst input and counter-blowing burst input have the similar characteristics of the instantaneous flow fields, burst mode input seems to enhance the instability of the shear layer regardless of the direction of the induced flow. In the counter-blowing normal input case, it is expected that separation is suppressed by another mechanism except above because counter-blowing normal input should steal the momentum of the free stream, and does not have the factor that the burst mode input has. Considering the fine three-dimensional vortices near the leading edge, it is expected that large momentum addition with high D_c value to the upstream direction disturbs the flow and make it become turbulence.

3.3 Comparison with experiments

In this subsection, the results of CFD simulations are compared with those of experiments[1]. The experiments were conducted with the condition of $\alpha = 12$deg. Therefore, we only discuss about the qualitative phenomena, not quantitative things. The experiments concluded that re-attach point of the flow moves to upstream direction in burst mode input cases, and counter-blowing burst input is more effective than co-flow normal input and less effective than co-flow burst input in the viewpoint of the minimum voltage at which separation can be suppressed. In this experiments, counter-blowing normal actuation has no effect for separation control. In order to check above things, below additional cases are conducted. First, the separation point and re-

Table 2 Additional computational cases

	P/A geometry	drive mode [Hz]	D_c
COF-N10	co-flow	normal	10
COF-N16	co-flow	normal	16
INV-N10	counter-blowing	normal	10
INV-N16	counter-blowing	normal	16
INV-B10	counter-blowing	burst	10
INV-B16	counter-blowing	burst	16

attach point, which are predicted from the C_f distributions of each case, are shown in Figs. 13 and 14. In the COF-N8, COF-N10, INV-N8 and INV-N10 cases, the flow separates from the airfoil and does not reattach. In the other cases, the flow reattaches. Comparing the COF-N12 and COF-N16 cases, both the separation point and reattach point move to downstream direction with increasing D_c value. This is because the momentum addition becomes larger and turbulent transition delays. On the other hand, in the co-flow burst input cases, reattach points move to upstream direction with increasing D_c value, where separation points barely move. Almost the same tendency can be seen in the counter-blowing burst input cases except the INV-B8 case, in which separation is not fully suppressed. These results corresponds to the those of the experiments. In the cases of the counter-blowing normal input in which separation is fully suppressed, relatively small separated region can be seen in Fig. 14. This might be because flow disturbs by the large momentum addition and quickly transit to turbulence.

In this computational study, counter-blowing normal actuation with large D_c can suppress separation, where it cannot in the experiments. This

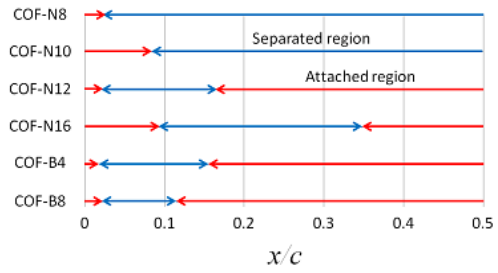

Fig. 13 Separated regions and attached regions of co-flow input cases.

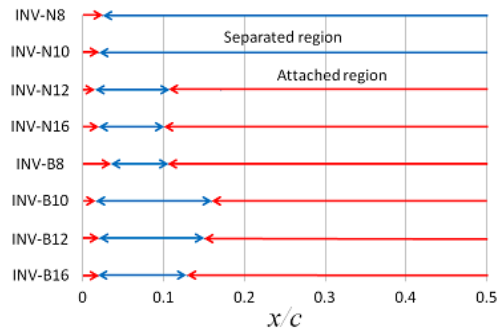

Fig. 14 Separated regions and attached regions of counter-blowing input cases.

is because the body force with $D_c = 12, 16$ seems to be much larger than that of the actuator which is used in the experiments. In the preliminary experiments, we check that the plasma actuator we use can induce velocity up to $2m/s$ in static air. This corresponds to 20% free stream speed in this Reynolds number condition. We also check that the body force with $D_c = 12, 16$ can induce almost the same velocity as the free stream. This means that counter-blowing burst actuation in this simulation requires larger momentum for separation control than that in the experiments. This difference seems to be occurd by the difference of the angle of attack and the geometry of the body force.

4 Conclusions

Four types of cases in which the body force is added over an NACA0015 airfoil in co-flow normal input, co-flow burst input, counter-blowing normal input and counter-blowing burst input are simulated by implicit large eddy simulations using a high resolution compact scheme. In all the cases except counter-blowing normal input case, the two-dimensional vortices are generated from the leading edge then become complex three-dimensional vortices. It is verified that the characteristics of separation control between co-flow burst input and counter-blowing burst input are almost the same. This implies that the mechanisms of burst actuation for separation control are the same regardless of the direction of the induced flow. In both co-flow burst actuation case and counter-blowing burst actuation case, the two-dimensional vortices become three-dimensional vortices more quickly than co-flow normal actuation case. This is because burst mode actuation enhance the instability of the shear layer regardless of the direction of the induced flow. On the other hand, in counter-blowing normal case, complex three-dimensional vortices are generated from the leading edge. This is because the large momentum addition disturbs the flow directly without making use of Kelvin-Helmholtz instability.

Also, the results of the simulation in this study are compared with the experiments[1]. Focusing on the reattach point, in both burst cases, the reattach point moves to upstream with increasing D_c value. This result is consistent with that of the experiments.

5 Copyright Statement

References

[1] Satoshi Sekimoto, Kengo Asada, Masayuki Anyoji, Taku Nonomura, and Kozo Fujii. Comparative study of co-flow and counter blowing dbd plasma actuators for separated flow over an airfoil. In *AIAA 2012-1137*, 2012.

[2] C. L. Enloe, T. E. McLaughlin, R. D. VanDyken, K. D. Kachnew, E. J. Jumper, and T. C. Corke. Mechanisms and responses of a single dielectric barrier plasma actuator: Plasma morphology. *AIAA J.*, 42:589–594, 2004.

[3] C. L. Enloe, T. E. McLaughlin, R. D. VanDyken, K. D. Kachnew, E. J. Jumper, T. C. Corke, M. Post, and O. Haddad. Mechanisms and responses of a single dielectric barrier plasma actuator: Geometric effects. *AIAA J.*, 42:595–604, 2004.

[4] T. C. Corke and M. L. Post. Overview of plasma flow control: Concepts, optimization, and applications. In *AIAA2005-563*, 2005.

[5] T. C. Corke, C. L. Enloe, and S. P.Wilkinson. Dielectric barrier discharge plasma actuators for flow control. In *Annual Review of Fluid Mechanics*, 2010.

[6] D. Greenblatt, B. Göksel, C. Y. Schüle, D. Romann, and C. O. Paschereit. Dielectric barrier discharge flow control at very low flight reynolds numbers. *AIAA J.*, 46:1528–1541, 2008.

[7] B. Göksel, D. Greenblatt, I. Rechenberg, C. N. Nayeri, and C. O. Paschereit. Steady and unsteady plasma wall jets for separation and circulation control. In *AIAA2006-3686*, 2006.

[8] T. Nonomura, S. Sekimoto, K. Asada, A. Oyama, and Fujii K. Experimental study of blowing direction effects of dbd plasama actuator on separation control of flow around an airfoil. In *AJK2011-15010*, 2011.

[9] M. R. Visbal and D. V. Gaitonde. Control of vortical flows using simulated plasma actuators. In *AIAA 2006-505*, 2006.

[10] C. O. Porter, T. E. McLaughlin, C. L. Enloe, G. I. Font, J. Roney, and J. W. Baughn. Boundary layer control using a dbd plasma actuator. In *AIAA 2007-786*, 2007.

[11] Y. B. Suzen and P. G. Huang. Simulations of flow separation control using plasma actuator. In *AIAA 2006-877*, 2006.

[12] K. Fujii. Developing an accurate and efficient method for compressible flow simulations-example of cfd in aeronautics. In *Proceedings of the 5th International Conference on Numerical Ship Hydrodynamics*, 1990.

[13] S. Obayashi, K. Matsushima, K. Fujii, and K. Kuwahara. Improvements in efficiency and reliability for navier-stokes computations using the lu-adi factorization algorithm. In *Proceeding of the 24th AIAA Aerospace Science Meeting, New York, USA*, 1986.

[14] S. K. Lele. Compact finite difference scheme with spectral-like resolution. *Journal of Computational Physics*, 103:16–42, 1992.

[15] M. R. Visbal and D. V. Gaitonde. Computation of aeroacoustic field on general geometries using compact differencing and filtering schemes. In *AIAA 1999-3706*, 1999.

[16] D. V. Gaitonde and M. R. Visbal. Pade-type higher-order boundary filters for the navier-stokes equations. *AIAA Journal*, 38:2103–2112, 2000.

[17] H. Nishida and T. Nonomura. Adi-sgs scheme on ideal magnetohydrodynamics. *Journal of Computational Physics*, 228:3182–3188, 2009.

[18] M. R. Visbal and D. P. Rizetta. Large-eddy simulation on general geometries using compact differencing and filtering schemes. In *AIAA 2002-288*, 2002.

[19] K .Fujii. United zonal method based on the fortified solution algorithm. *Journal of Computational Physics*, 118:92–108, 1995.

[20] K. Asada and K. Fujii. Computational analysis of unsteady flow-field induced by plasma actuator in burst mode. In *AIAA2010-5090*, 2010.